Energy Storage Materials 22 (2019) 120–127

Contents lists available at ScienceDirect

Energy Storage Materials

journal homepage: www.elsevier.com/locate/ensm

Potassium nickel hexacyanoferrate as cathode for high voltage and ultralong life potassium-ion batteries

Shaokun Chong [a,b], Yifang Wu [d], Shengwu Guo [a], Yongning Liu [a,**], Guozhong Cao [c,*]

[a] State Key Laboratory for Mechanical Behavior of Materials, School of Material Science and Engineering, Xi'an Jiaotong University, Xi'an, 710049, PR China
[b] John A. Paulson School of Engineering and Applied Sciences, Harvard University, Cambridge, MA, 02138, United States
[c] Department of Materials and Engineering, University of Washington, Seattle, WA, 98195-2120, United States
[d] Northwest Institute for Nonferrous Metal Research, Xi'an, 710016, PR China

ARTICLE INFO

Keywords:
Potassium-ion battery
Potassium nickel hexacyanoferrate
Cathode materal
Zero-strain
Ultralong life

ABSTRACT

Potassium-ion batteries (KIBs) are considered as one of the most promising energy storage devices owing to the close redox potential to lithium, rich abundance and low cost potassium resource, promoting the exploration on cathode materials for K-ions storage. This paper reports a detailed experimental study on potassium nickel hexacyanoferrate, $K_{1.81}Ni[Fe(CN)_6]_{0.97}\cdot 0.086H_2O$ (KNHCF), cathode for KIBs. KNHCF synthesized possesses few $[Fe(CN)_6]^{4-}$ vacancies and coordinated water molecules, and high specific surface area along with developed microporous/mesoporous structures, which collectively induce highly reversible electrochemical intercalation process and fast kinetics. The resultant KNHCF cathode demonstrates reversible capacity of 57.0 $mAh\cdot g^{-1}$, high operating voltage of 3.74 V, outstanding voltage stability with no decay, good cycling stability (87.34%) after 1000 cycles and long-term lifetime over 8000 cycles with capacity fading rate of 0.0052% per cycle. A solid solution mechanism with zero-strain, where one-electron shuttle relied on C-coordinated Fe^{II}/Fe^{III} couple, plays an important role for K-ions intercalation/deintercalation. A 3.34 V full cell assembled with graphite anode delivers a high energy density of 142.6 $Wh\cdot kg^{-1}$ with the cpacity retention of 88.5% after 100 cycles, and ultra-long life-span over 5000 cycles can be achieved.

1. Introduction

Advanced electric energy storage (EES) systems can effectively regulate and reduce energy consumption and environmental degradation by integrating the intermittent renewable energy into smart power grids [1,2]. Nowadays, rechargeble lithium-ion batteries (LIBs), one of the major EES technologies, have dominated the market for portable electronic devices and electric vehicles owing to its high energy density and long cycling life [3–5]. However, large-scale stationary applications for LIBs are limited by the short supplies and high cost of lithium resource, which has motivated the development of new types of rechargeable batteries with abundant reserve. As alternatives to LIBs, numerous alkali-ion batteries including Na, K, Mg, Zn, Ca and Al, based on earth abundant elements, have been studied in-depth, which expand new members for cost effective EES [6–11]. To date, unprecedented progress has been achieved by investigating the electrode materials and electrochemical mechanism for sodium-ion batteries (NIBs) [12–18]. However, KIBs possess a significant advantage of low redox potential of −2.93 V for K/K^+ vs. the standard hydrogen electrode (SHE), close to that of −3.04 V for Li/Li^+ and lower than −2.71 V for Na/Na^+ (vs. SHE), which can output higher voltage and energy density compared to NIBs [19]. It was reported that graphite electrode, successfully developed in the field of LIBs, can be employed as anode for KIBs [20,21], which is another important advantage over NIBs. Furthermore, other new anode materials such as soft and hard carbon [22,23], alloying mechanism materials (P, Bi, Sn and Sb) [24–29], transition metal oxides [30], sulfides, carbides and selenides [31–34], organics as well as K–Na alloy are also proved as anode electrodes for KIBs [35–37], displaying great electrochemical properties and further promoting the development of KIBs.

Exploring advanced cathode materials with excellent structure stability is a key issue for the advancement of K-ion full-cells due to the restriction of the larger ionic radius of K-ion (1.38 Å) compared to Li-ion (0.76 Å) and Na-ion (1.02 Å). Layered metal oxides (such as $K_{1.06}Mn_8O_{16}$, $K_{0.32}MnO_2$, $K_{0.7}Fe_{0.5}Mn_{0.5}O_2$, $K_{0.6}CoO_2$ and $K_{0.5}MnO_2$) as well as

* Corresponding author.
** Corresponding author.
E-mail addresses: ynliu@mail.xjtu.edu.cn (Y. Liu), gzcao@uw.edu (G. Cao).

https://doi.org/10.1016/j.ensm.2019.07.003
Received 7 April 2019; Received in revised form 11 June 2019; Accepted 1 July 2019
Available online 4 July 2019

polyanionic compounds with open framework (such as $FePO_4$, KVP_2O_7 and $KVPO_4F$) have been investigated as intercalation cathodes for nonaqueous KIBs, while limited interlayer distance and clearance space make difficulty in K-ions storage, which gives rise to unsatisfactory electrochemical properties [38–45]. In addition, organic electrodes with large primary interlayer spacing break through the traditional intercalation limit by utilizing strong electron-withdrawing groups on the edges of fused aromatic rings for K-ions storage, which can provide high energy density because of multiple active sites [46,47]. Whereas an inevitable drawback of organic electrode is free K-ions in original material, which makes anode materials need to provide enough K-ions in full-cell system. Recent years, numerous efforts have been devoted to Prussian blue and its analogues as cathodes for aqueous and nonaqueous PIBs, whose long cycling life is ascribed to stable open framework structure with large interstitial sites and reversible electrochemistry [45–53], pointing out the direction of designing new cathode materials to realize repeatable insertion/extraction processes of large-size K-ions.

In this paper, we reported a comprehensive research on $K_{1.81}Ni[Fe(CN)_6]_{0.97}\cdot 0.086H_2O$ (KNHCF) cathode for KIBs. High first capacity of 57.0 mAh·g^{-1} with the energy density of 213.2 Wh·kg^{-1} at 10 mA g^{-1}, eminent cyclability and rate performance at various rates can be obtained for KNHCF. It is also demonstrated by ex situ XRD and XPS analyses that K-ions intercalation/deintercalation proceed through a simple solid solution reaction. And the superior electrochemcial properties are attributed to ultra-stable framework structure, highly reversible electrochemical behavior and fast electrons transfer and K-ions dissfusion ability. K-ions full cell is also fabricated based on graphite as anode, exhibiting satisfactory discharge capacity and outstanding cycling stability for 5000 cycles.

2. Experimental

2.1. Material preparation

The KNHCF was prepared via a facile hydrothermal approach using 5 mmol $K_4Fe(CN)_6\cdot 3H_2O$ and 5 mmol $Ni(NO_3)_2\cdot 6H_2O$ as the starting chemicals. After dissolving in 70 mL deionized water completely under continuous magnetic stirring, the uniform solution was transferred to a 100 mL Teflon-lined stainless steel autoclave, which was further heated at 80 °C for 12 h. After cooling down naturally, the sample was collected through high-speed centrifugation, washing with deionized water and ethanol several times, and freeze-drying for 48 h. For comparison, potassium copper hexacyanoferrate (KCHCF) powder was also synthesized by the above procedure using $CuCl_2\cdot 2H_2O$ instead of $Ni(NO_3)_2\cdot 6H_2O$.

2.2. Material characterization

Inductively coupled plasma atomic emission spectroscopy (ICP-AES, Optima 7300DV, PerkinElmer) and elemental analyzer (vaeeio MACRO cube, Elementar) were conducted to examine the exact chemical compositions. The contents of adsorbed and coordinated water in PBAs crystal were dertermined by thermogravimetry (TG) analysis measured on TGA/DSC3+instrument (Mettle Toledo) from room temperature to 550 °C with a heating rate of 10 °C·min^{-1} under a flowing N_2. Raman spectrometer (HR 800, JY Labram) and Fourier transform infrared (FTIR) spectrometer (Vetex 70, Bruker) were employed to record the Raman and FTIR spectra. X-ray photoelectron spectroscopy (XPS, Axis Ultrabld, Kratos) was performed to analyze the detailed information of valence states for transition metals. The crystal structure and phase purity were investigated by X-ray diffraction (XRD) on Rigaku UltimaIV-185 with Cu Ka radiation at 40 mA and 40 kV, and the XRD pattern was refined on the basis of the Rietveld refinement program GSAS. The N_2 adsorption-desorption measurement was carried out on Micromeritics ASAP 2460 analyzer. Transmission electron microscope (TEM, JEOL JEM- 2100CX) was measured to observe the morphology and study the microstructure of sample, and equipped energy dispersive spectra (EDS) was used to acquire the elemental mapping.

2.3. Electrochemical tests

CR2025-type coin cells were utilized to assemble the half-cells to evaluate the electrochemical performances of cathodes in an Ar-filled glove box (Super 1220/750, Mikrouna), where the glass fiber, K metal disk and 1 M KPF_6 in ethylene carbonate, diethyl carbonate and propylene carbonate (1: 1: 1 by volume) were respectively regarded as separator, counter electrode and electrolyte. The cathode electrode was fabricated via spreading the slurry onto the surface of Al foil, where the homogeneous slurry was formed by mixing the active material, acetylene black and polyvinylidene fluoride with the mass ratio of 8:1:1 in N-methyl pyrrolidinone. After drying at 60 °C for 12 h under vacuum and pressing for densification, the Al foil was further punched into sheets with the diameter of 12 mm to obtain the working electrodes. The weight loading of active material were controlled from 1.5 to 2 mg. The K-ions full cell was assembled with graphite on Cu foil as anode, whose mass ratio of cathode/anode was approximately 1:2. The half and full cells were charged/discharged at 25 °C in the potential range of 2.0–4.5 V (vs. K/K^+) at various current densities (1C = 70 mA g^{-1}).

Cyclic voltammetry (CV) and electrochemical impedance spectroscopy (EIS) were tested on a CHI 660C electrochemistry workstation. The galvanostatic intermittent titration technique (GITT) was conducted to calculate the K-ion diffusion coefficient, which is obtained from the potential response to a constant current pulse (10 mA g^{-1}), and the batteries were charged for 600 s followed by open-circuit relaxation for 3600 s. The electrode was acquired via disassembling the coin-cells after charging/discharging at different cut-off potentials or several cycles. By washing with diethyl carbonate and drying in the glove box, the active material was further measured through ex situ XRD and XPS to study the electrochemical mechanism and structure stability.

3. Results and discussion

3.1. Structure and morphology

The chemical formulas of KCHCF and KNHCF can be determined to be $K_{1.72}Cu[Fe(CN)_6]_{0.83}\cdot 0.887H_2O$ and $K_{1.81}Ni[Fe(CN)_6]_{0.97}\cdot 0.086H_2O$ according to ICP-AES, elemental analyses (Tables S1–S2) and TG results (Figs. S1–S2), suggesting that there is few $[Fe(CN)_6]^{4-}$ vacancies and coordinated water molecules for KNHCF compared to KCHCF, which is conducive to activate more Fe redox sites coordinated by C atoms and stabilize the framework structure for acquiring higher capacity and more exceptional cycling stability [13]. Fig. 1a presents the FTIR spectra of KCHCF and KNHCF, in which the peaks at 1630 cm^{-1} and 3435 cm^{-1} are assigned to the bending and stretching modes of O–H [51], respectively, indicating the presence of adsorbed water, which is also observed from the TG curves. Besides, the peaks at 2095 cm^{-1} associated with C≡N appear. In the Raman spectra from 200 cm^{-1} to 3000 cm^{-1}, peaks located at 245 cm^{-1} and 510 cm^{-1} for KCHCF (Fig. S3) as well as 271 cm^{-1} and 540 cm^{-1} for KNHCF (Fig. S4), respectively corresponding to stretching and bending modes of Fe–C≡N–Cu and Fe–C≡N–Ni [10,48], are observed. And there are other peaks at 2138 cm^{-1} and 2097 cm^{-1} (KCHCF) as well as 2154 cm^{-1} and 2116 cm^{-1} (KNHCF), which are ascribed to cyanogen [48,51].

The porous features of both samples were analyzed by the N_2 adsorption/desorption measurement in Fig. 1b. It can be seen from the inset of Fig. 1c that the sample contains developed micropore structure for K-ions storage, which are mainly distributed within the range of 3.5–5.1 Å, corresponding to the interstitial sites of the framework. Meanwhile, the much higher BET specific surface area of 168.2 m^2 g^{-1} for KNHCF compared to KCHCF (145.7 m^2 g^{-1}) along with interconnected mesoporous structure around 3.4 nm (Fig. 1c) are beneficial for the fast K-ions diffusion and effective electrolyte immersion. The surface chemical composition and electronic states of both samples were

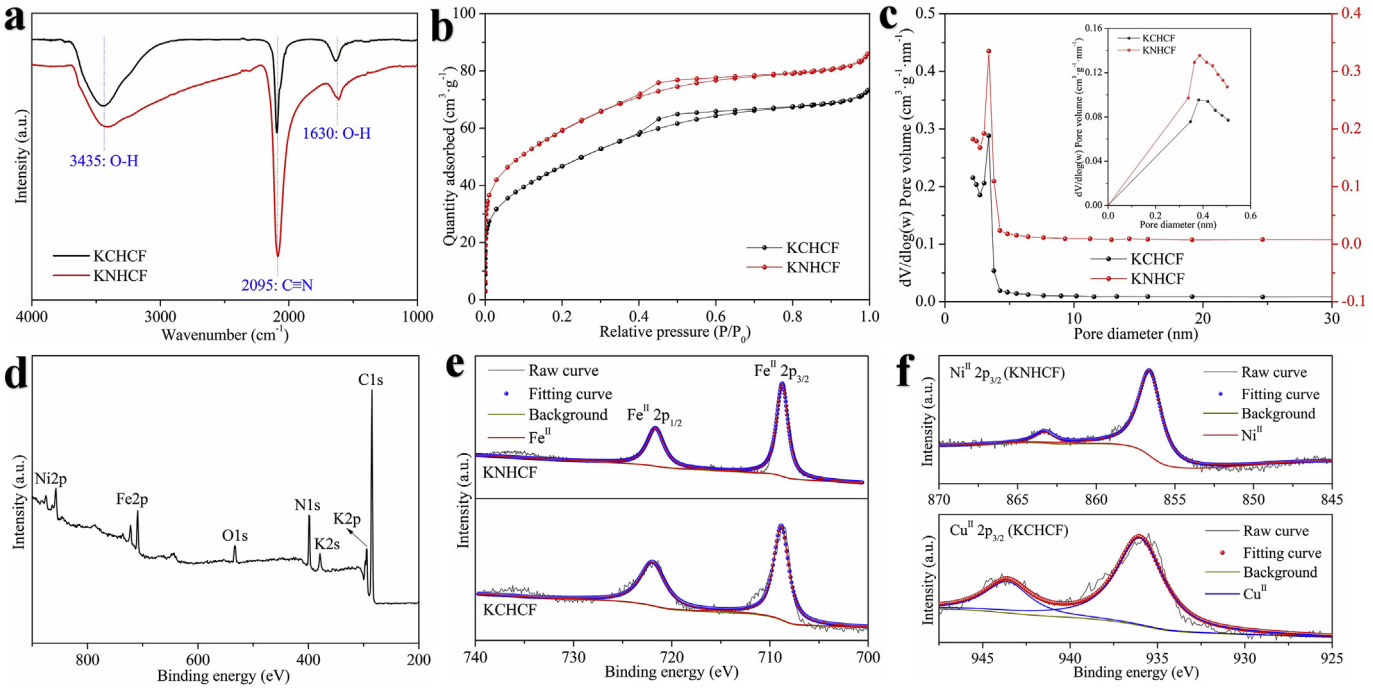

Fig. 1. Structure characterization of samples: a) FTIR spectra; b) nitrogen adsorption-desorption isotherms; c) mesoporous size distribution profiles, inset are the micropore size distribution curves of KCHCF and KNHCF; d) XPS survey spectrum of KNHCF; e) Fe 2p spectra of both samples, f) Cu $2p_{3/2}$ spectrum of KCHCF and Ni $2p_{3/2}$ spectrum of KNHCF.

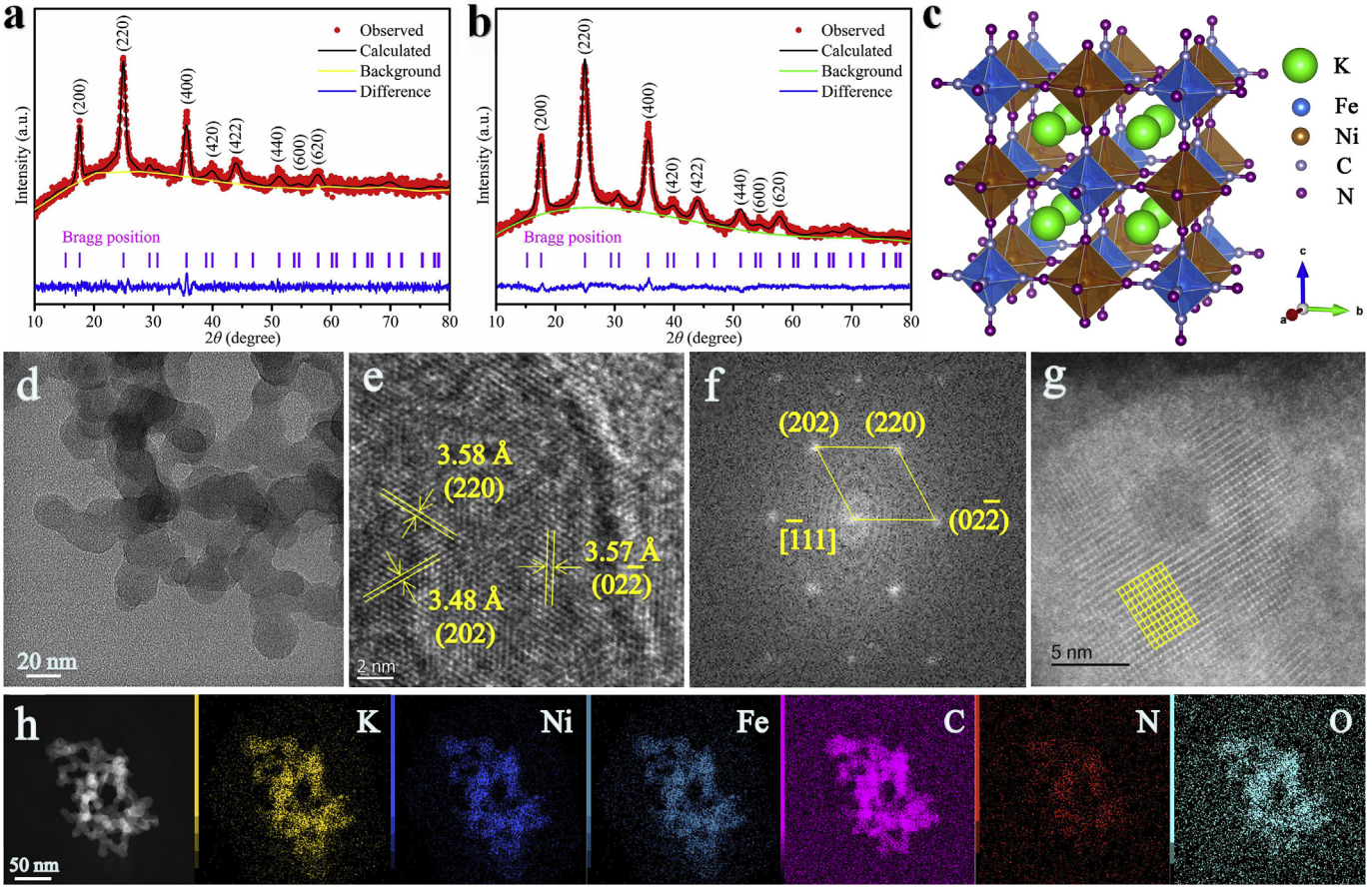

Fig. 2. Structure and morphology characterization: Rietveld refinement XRD patterns of a) KCHCF with the convergence factors of $\chi^2 = 1.120$, $R_{wp} = 1.27\%$, $R_p = 1.00\%$ and b) KNHCF ($\chi^2 = 0.854$, $R_{wp} = 1.41\%$, $R_p = 1.12\%$); c) the refined structural model; d) TEM image; e) HRTEM image; f) FFT pattern; g) high resolution HAADF-STEM image and h) EDS mapping images of KNHCF.

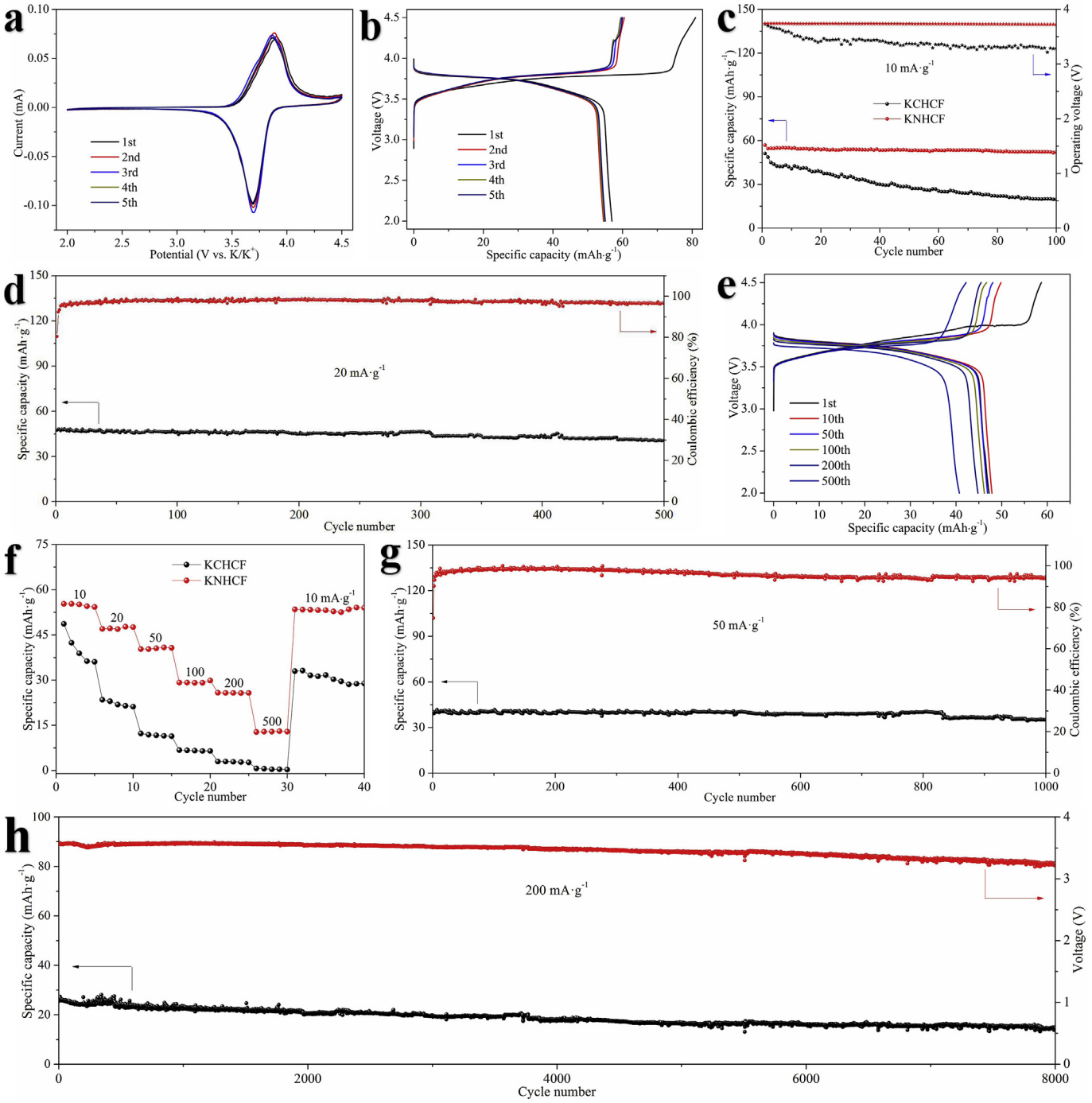

Fig. 3. Electrochemical performances: a) CV profiles of the first five cycles for KNHCF at a scanning rate of 0.1 mV s^{-1}; b) corresponding galvanostatic charge/discharge curves at 10 mA g^{-1}; cycling performances at c) 10 mA g^{-1} for both samples and d) 20 mA g^{-1} for KNHCF; e) galvanostatic charge-discharge profiles for the 1st, 10th, 50th, 100th, 200th and 500th cycles at 20 mA g^{-1} for KNHCF; f) rate property at different rates from 10 to 500 mA g^{-1}; cycling performances at g) 50 mA g^{-1} and h) 200 mA g^{-1} for KNHCF.

tested by XPS, and the survey spectra in Fig. S5 (KCHCF) and Fig. 1d (KNHCF) indicate that the sample contains K, Cu/Ni, Fe, C, N, and O elements. The high resolution (HR) fitting spectra of Fe are shown in Fig. 1e, where the peaks centered at 708.7 eV and 721.7 eV are attributed to Fe^{II} $2p_{3/2}$ and Fe^{II} $2p_{1/2}$, respectively. The Ni 2p spectrum of KNHCF exhibits the binding energies of 856.6 eV and 863.3 eV for Ni^{II} $2p_{3/2}$ as displayed in Fig. 1f, and another couple around 874.5 eV and 881.0 eV correspond to Ni^{II} $2p_{1/2}$ in Fig. S6. Besides, the fitting results of Cu $2p_{3/2}$ (Fig. 1f) and Cu $2p_{1/2}$ (Fig. S7) spectra for KCHCF also suggest that Cu-ions are divalent.

The XRD patterns of both samples (Fig. S8) are refined using Rietveld method as presented in Fig. 2a (KCHCF) and Fig. 2b (KNHCF), which are assigned to face-centered cubic (FCC) structure with the space group of Fm3 m [51,53,54]. The detailed refinement results in Table S4 indicates that KNHCF has the lattice parameters of a = b = c = 10.219 Å, which are higher than that of a = b = c = 10.104 Å for KCHCF (Table S3), and the average crystalline sizes can be determined as 18.3 nm (KNHCF) and 19.6 nm (KCHCF) calculated by Scherer equation. Fig. 2c displays the corresponding structure illustration of KNHCF, in which a 3D framework with large interstitial sites is built by bridging nitrogen and carbon atoms

of cyanogen ligands with Ni and Fe ions, respectively.

The morphology and microstructure of KNHCF were investigated by TEM. As presented in Fig. 2d, KNHCF is composed of homogeneous nanoparticles with the size of 15–25 nm, which is in favor of K-ions and electrons transport compared to the reported PBAs particles with larger size [48,52]. Distinct lattice fringes can be seen from HRTEM image in Fig. 2e, in which the interplanar spacings of 3.58 Å, 3.57 Å and 3.48 Å are respectively assigned to (220), (022) and (202) planes of cubic structure. The corresponding Fast Fourier Transformation (FFT) pattern in Fig. 2f can be indexed to [1 11] zone axis, which is consistent with the HRTEM result. Fig. 2g gives the high resolution HAADF-STEM image of KNHCF, exhibiting obvious rectangular interstitial sites. The EDS elemental mapping image in Fig. 2h further proves the uniform distribution of K, Ni, Fe, C, N and O elements.

3.2. Electrochemical performances

The electrochemical properties were investigated between 2.0 and 4.5 V as exhibited in Fig. 3. CV measurement was conducted to provide insights into the electrochemical process and reversibility at a scanning rate of 0.1 mV s^{-1}. KNHCF displays a pair of redox peaks of 3.90/3.69 V during the initial process in Fig. 3a, and a couple of peaks (4.04/3.71 V) appear for KCHCF in Fig. S9a, which are attributed to the oxidation/reduction of low-spin Fe^{II}/Fe^{III} couple (Fe^{LS}) coordinated by C atoms [10]. During K-ions extraction from the π-electron coordination environment in the interstitial sites, the Fermi energy level will decrease toward valence bands of Fe t_{2g} resulted from the electrons transfer, thus exhibiting electrochemical activity for C-linked Fe-ions [57]. However, there is much more difficult charge transfer behavior because the 3d states of Ni-ions are situated far below the Fermi level, making high-spin Ni-ions (Ni^{HS}) are electrochemical inert [57]. Fig. 3b shows the corresponding galvanostatic charge/discharge profiles of KNHCF at 10 mA g^{-1}, in which a set of plateaus in the range of 3.44–3.88 V can be observed, in consistent with the CV result. It is worth mentioning that the redox peaks and plateaus for KNHCF remain almost unchanged in the following cycles, revealling no polarization and highly reversible redox behavior, while terrible polarrization can be seen from the subsequent CV and charge-discharge curves of KCHCF in Fig. S9.

A reversible initial discharge capacity of 57.0 mAh·g^{-1} with high operating potential of 3.74 V at 10 mA g^{-1} can be acquired for KNHCF, delivering an energy density of 213.2 Wh·kg^{-1}, which is higher than that of KCHCF (191.0 Wh·kg^{-1}) with the capacity of 51.2 mAh·g^{-1} and voltage of 3.73 V. Fig. S10 compares the operating voltages and specific capacities of the most reported cathode materials based on one-electron transfer with KNHCF, in which the highest energy density can be achieved for KNHCF [58–60,64,74]. And the excellent cycling stability with the capacity retention of 52.1 mAh·g^{-1} (91.4%) and exceptional voltage stability with no fading after 100 cycles are obtained for KNHCF as shown in Fig. 3c, while KCHCF suffers serious capacity fading with the capacity retention rate of 38.48% and rapid voltage decay with the value of 0.438 V. Besides, KNHCF delivers high first discharge capacity of 47.2 mAh·g^{-1} at 20 mA g^{-1} with the retention of 40.7 mAh·g^{-1} (86.23%) over 500 cycles in Fig. 3d, uncovering outstanding capacity stability. The values of coulombic efficiency can reach approximately 100% after the first cycle at 20 mA g^{-1}, revealing that K-ions insert/extract reversibly in the intersititial sites. Fig. 3e displays the charge/discharge curves at 20 mA g^{-1}, where no distinct change for the voltage plateaus can be seen, suggesting remarkable voltage (Fig. S11) and structure stability during cycling.

The rate capability was tested in the range of 10–500 mA g^{-1} as shown in Fig. 3f, which can provide the capacities of 55.3, 47.7, 40.9, 29.9, 25.8 and 13.1 mAh·g^{-1} for KNHCF at 10 (0.14C), 20 (0.29C), 50 (0.71C), 100 (1.4C), 200 (2.9C) and 500 mA g^{-1} (7.1C). However, much lower capacities of 48.7, 23.5, 12.3, 6.8, 3.0 and 0.7 mAh·g^{-1} are acquired for KCHCF. The reversible capacity of 53.5 mAh·g^{-1} for KNHCF, much higher than that of KCHCF (33.2 mAh·g^{-1}), can be maintained when the rate returns back to 10 mA g^{-1}. We further evaluate the long-term cycling performances of KNHCF at high current densities. The capacity of 35.2 mA g^{-1} can be maintained over 1000 cycles with the capacity retention rate of 87.34% at 50 mA g^{-1} in Fig. 3g, and KNHCF discloses ultra-long cycling life for 8000 cycles at 200 mA g^{-1} (Fig. 3h), delivering ultra-low capacity fading of 0.0052% per cycle and great cyclability.

3.3. Electrochemical reaction mechanism

In order to better clarify the electrochemical reaction mechanism and redox active sites for K-ions storage of KNHCF, we employed ex situ XRD and XPS tests at different states during the initial charge/discharge process (Fig. 4a). The ex situ XRD patterns are shown in Fig. 4b, where the cubic structure can be maintained well during the charge/discharge process, demonstrating that there is a facile solid solution mechanism for K-ions extraction/insertion rather than phase change [51,53]. The shift of calculated lattice parameter in Fig. 4c is negligible, suggesting ultra-stable framework structure with zero-strain for K-ions storage. Fig. 4d displays the ex situ XPS of Ni 2p spectra, where all the curves remain almost the same, uncovering that Ni^{HS} coordinated by N atoms are electrochemically inert, which is in favor of maintaining the super-stable structure during cycling. However, in the ex situ Fe spectra (Fig. 4e), the peaks of Fe2p gradually shift to higher positions along with the deintercalation of K-ions during the charge process and Fe^{II} can be oxidized to Fe^{III} at the full charge state, which indicates that Fe^{LS} couple linked by C atoms are regarded as redox center for K-ions insertion/extraction. And an opposite behavior occurs upon the discharge process, proving superior electrochemical reversibility based on Fe^{II}/Fe^{III} redox sites.

The solid state diffusion kinetics of K-ions for samples was studied by GITT measured at 10 mA g^{-1} for the initial charge process as displayed in Fig. 4f. It can be calculated that the K-ions diffusion coefficient (D_K^+) during the plateau region for KNHCF is from 10^{-9} to 10^{-7} cm^2 s^{-1} in Fig. 4g, which is one order of magnitude higher than that of KCHCF (between 10^{-10} and 10^{-8} cm^2 s^{-1}), exhibiting much faster K-ions transport ability in 3D framework for KNHCF. CV curves at various scanning rates in the range of 0.1–2.0 mV s^{-1} for both KCHCF and KNHCF were futher investigated to clarify the kinetics property. Serious polarization phenomenon can be observed for KCHCF in Fig. 4h, while the CV profiles (Fig. 4i) for KNHCF preserve the similar shapes with slight peak shifts with the increase of sweep rates, manifesting a splendid response capability to the fast scanning rates. The relationship between peak current (I_p) and scanning rate (v) can be described by the Randles-Sevcik equation of $I_p = 2.69 \times 10^5\ n^{3/2}\ A\ D^{1/2}\ C\ v^{1/2}$, where n, A, D and C are respectively stand for number of electrons, surface area of electrode, diffusion coefficient and concentration of K-ions [61]. Therefore, the D_K^+ can be dertermined by the simplified equation of $I_p = a\ D^{1/2}\ v^{1/2}$ (a is supposed to be the constant) [61]. Fig. 4j exhibits the fitting linear relationships between I_p and $v^{1/2}$, and the calculated slopes are the values of $a\ D^{1/2}$. Apparently, KNHCF electrode displays much higher K-ions diffusion coefficients for both oxidation and reduction processes than KCHCF, which is in accordance with the GITT result. Additionally, EIS results (Fig. S12) further prove that the charge-transfer resistance (R_{ct}) values of KNHCF are much lower compared to those of KCHCF before cycling, after 10 and 100 cycles, illuminating fast electrons transmission ability and developed K-ions transport paths.

The cubic phase of KNHCF can be well remained after 100 and 1000 cycles from the ex situ XRD results in Fig. S13, which suggests that KNHCF exhibits an extremely stable and robust 3D framework structure during repeated K-ions intercalation/deintercalation process. Hence, KNHCF undergoes a simple solid solution mechanism depended on $[Fe(CN)_6]^{4-}/[Fe(CN)_6]^{3-}$ one-electron redox couple, provides a stable cubic structure with few defects during cycling and presents extraordinary electrochemical kinetics and reversibility, thus resulting in exceptional cycling stability, which is the longest cycling lifetime among the

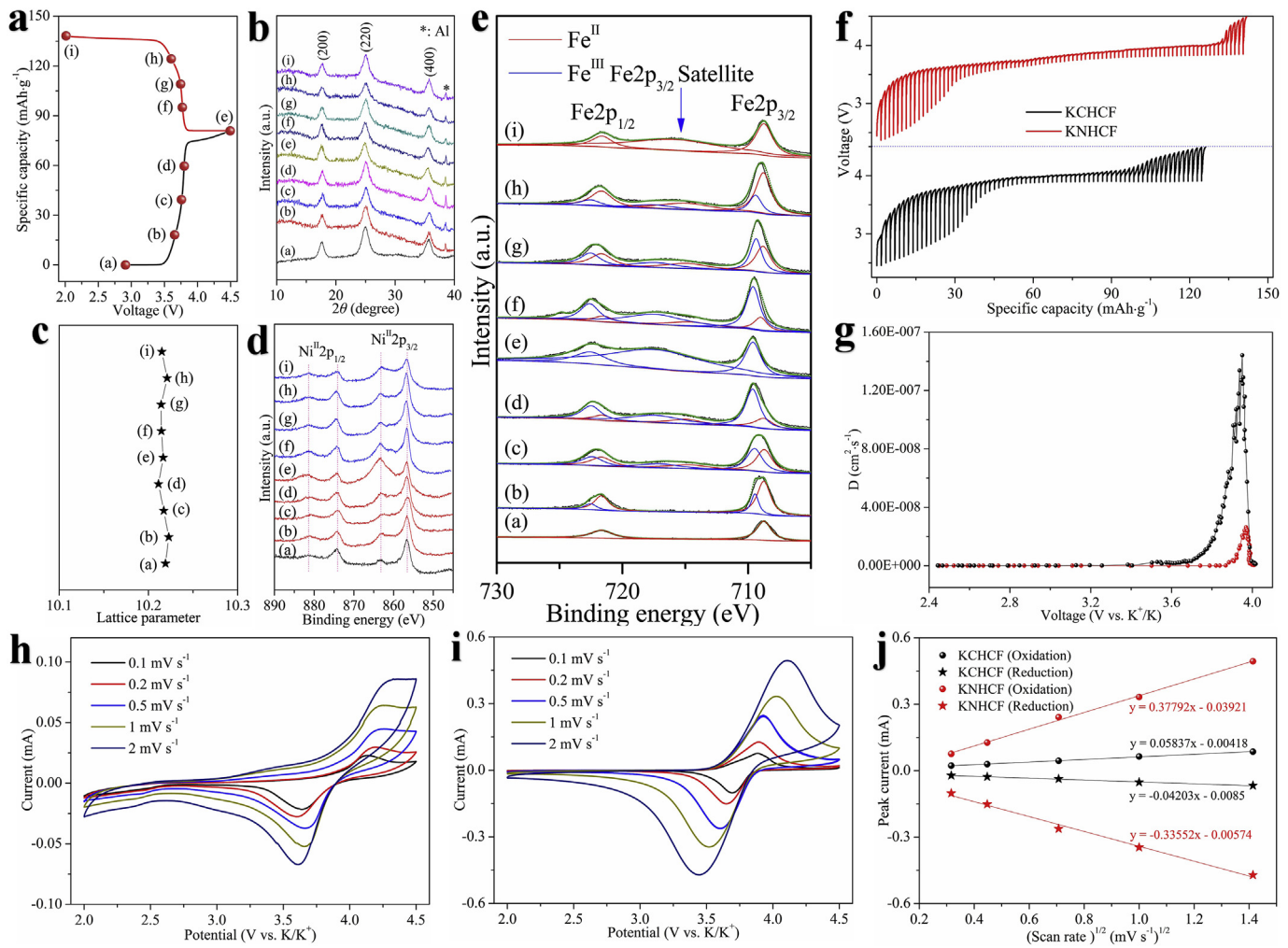

Fig. 4. Electrochemical mechanism of samples for potassium storage: a) the initial charge/discharge curve of KNHCF at 10 mA g^{-1}; b) the corresponding ex situ XRD patterns at different states; c) changes of lattice parameter calculated by XRD patterns; ex situ XPS spectra for d) Ni and e) Fe elements; f) GITT profiles of KCHCF and KNHCF, as well as g) corresponding K-ions diffusion coefficients; CV curves of h) KCHCF and i) KNHCF at different scanning rates; j) linear relationship between the peak current (I_p) versus the square root of the scanning rate ($v^{1/2}$) and the corresponding linear fits.

reported cathode materials for KIBs (Table S5) [38–42,44–47,51–53,55,56,62–75].

Although the significant enhancement in both storage capacity and transport kinetics are the subject for further research, the change of lattice constants and the decrease in vacancies and coordinated water molecules likely exerted their impacts through the following mechanisms: firstly, the expanded lattice parameters of KNHCF (a = b = c = 10.219 Å) induced by high content of K-ions in the interstitial sites in comparison with KCHCF (10.104 Å), beneficial to fast K-ions diffusion during cycling [76]. Secondly, the electrochemical activity of neighboring Fe^{LS} (C) for KCHCF is likely drastically degraded because its electronic structure was largely affected by vacancies and there is less available unoccupied states of Fe^{LS} (C) above the Fermi level, resulting in poor electronic conductivity compared with KNHCF [77]. Hence, the improved electrochemical performances for KNHCF compared with KCHCF is mainly ascribed to its optimized structure with less defects and high content of K-ions, which can not only activate more Fe^{II}/Fe^{III} redox couple, but also facilitate fast electrons and K-ions transport.

3.4. Full-cell performances

For the sake of practical feasibility of KNHCF cathode, K-ion full cell was fabricated with the graphite as anode, illustrated in Fig. 5a. The charge-discharge profiles of graphite are shown in Fig. S14. It should be noted that the graphite has to be potassiated via predischarge process with metallic potassium before assembling the full cell, which can supplement enough K-ions and eliminate the first irreversible capacity. Fig. 5b shows the CV profiles of the first four cycles for the full cell, where a couple of oxidation/reduction peaks of C–Fe^{II}/Fe^{III} located at 3.34/3.06 V appear. The corresponding charge/discharge curve at 10 mA g^{-1} in Fig. 5c displays obvious plateaus, presenting high operating voltage of 3.34 V, and high discharge capacity of 42.7 mAh·g^{-1} with the energy density of 142.6 Wh·kg^{-1} are acquired. Fig. 5d exhibits the cycling property of the full cell at 10 mA g^{-1}, maintaining high capacity of 37.8 mAh·g^{-1} after 100 cycles with the retention rate of 88.5%. The reversible capacities of 36.5, 24.8, 19.5 and 16.4 mAh·g^{-1} can be retained for the full cell when the current densities are 20, 50, 100 and 200 mA g^{-1} in Fig. 5e, indicating remarkable rate capability. Furthermore, the full cell can cycle for 200 cycles at 50 mA g^{-1} with no capacity loss as presented in Fig. 5f, disclosing superior cycling stability. And ultra-long cycle lifespan over 5000 cycles (Fig. 5g) at 100 mA g^{-1}, with the capacity decay rate of 0.0035% per cycle, can be obtained.

4. Conclusions

KNHCF nanoparticles synthesized via a hydrothermal method, presenting low defect, high specific surface area with desired porous structure, have demonstrated to be an excellent cathode for KIBs. KNHCF

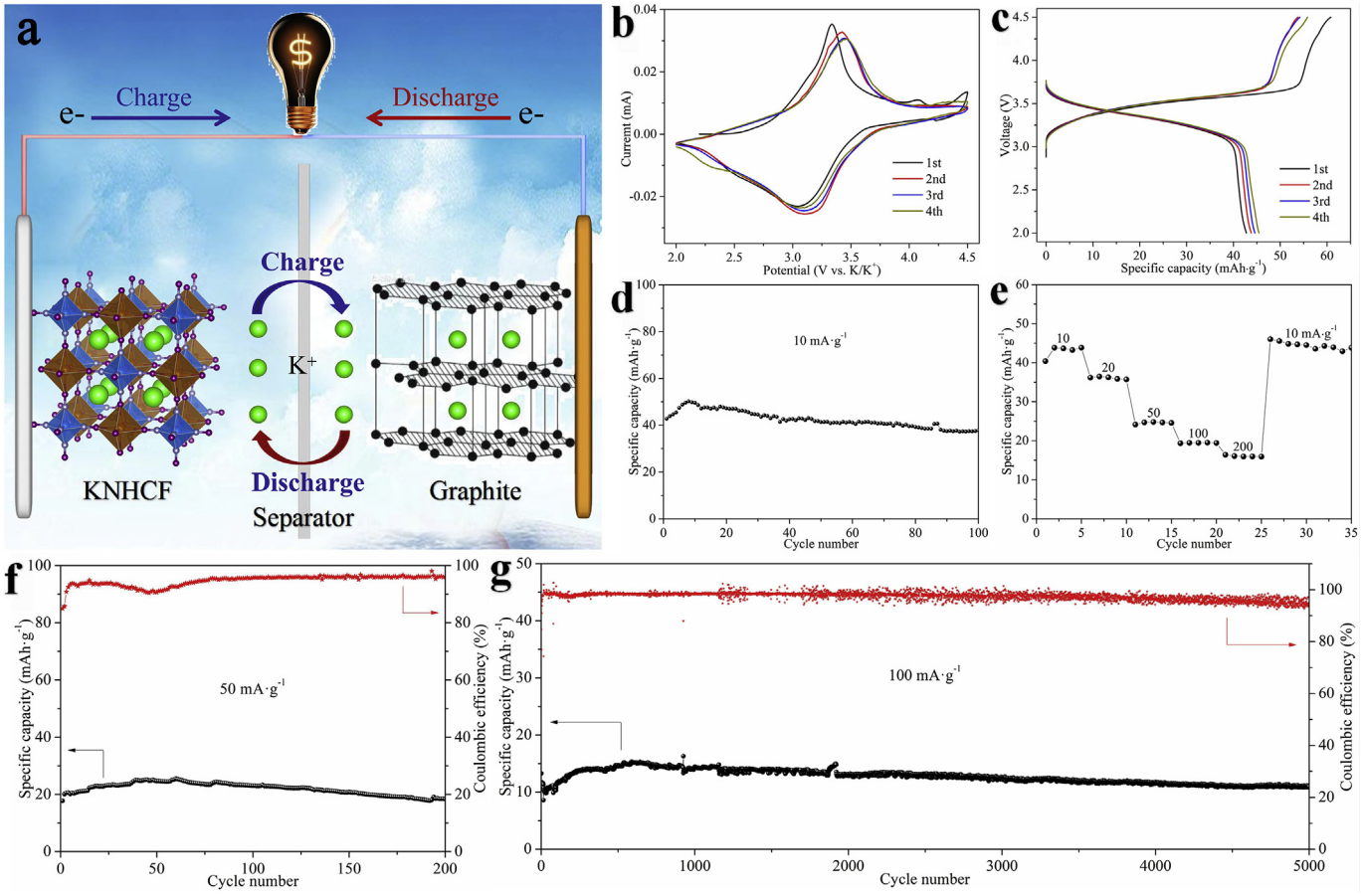

Fig. 5. Electrochemical properties of K-ions full cell based on KNHCF cathode and graphite anode: a) schematic view of the full cell; b) CV curves of the initial four cycles at the scanning rate of 0.1 mV s^{-1}; c) corresponding galvanostatic charge/discharge profiles at 10 mA g^{-1}; d) cycling performance at 10 mA g^{-1}; e) rate capability between 10 and 200 mA g^{-1}; cycling properties at high current densities of f) 50 mA g^{-1} and g) 100 mA g^{-1}.

delivered a reversible discharge capacity of 57.0 mAh·g^{-1} with a high operating voltage of 3.74 V at 10 mA g^{-1}, and excellent rate capability, unprecedented ultra-long life span over 8000 cycles at 200 mA g^{-1} was achieved. K-ions insert/extract to KNHCF through electrochemical intercalation reaction without structure transition based on one-electron active site of $[Fe(CN)_6]^{4-}/[Fe(CN)_6]^{3-}$, and the zero strain behavior prompts outstanding electrochemical kinetics and reversibility, as well as admirable structure stability upon cycling. K-ions full cell using graphite anode has shown a high energy density of 142.6 Wh·kg^{-1}, excellent cycling stability with the capacity retention of 88.5% after 100 cycles at 10 mA g^{-1}, and the longest cycling life for 5000 cycles ever reported in K-ions full cells. This work not only sheds light on the electrochemical mechanism of the zero-strain KNHCF cathode for K-ions storage, but also demonstrated the feasibility of K-ions full cell for the next generation EES system.

Acknowledgment

This work was supported by National Natural Science Foundation of China (No. 51504196), the Key Research and Development Plan of Shaanxi Province (Grant no. 2017ZDXMGY-039).

Appendix A. Supplementary data

Supplementary data to this article can be found online at https://doi.org/10.1016/j.ensm.2019.07.003.

References

[1] Z. Yang, J. Zhang, M.C.W. Kintner-Meyer, X. Lu, D. Choi, J.P. Lemmon, J. Liu, Chem. Rev. 111 (2011) 3577.
[2] K. Lin, Q. Chen, M.R. Gerhardt, L. Tong, S.B. Kim, L. Eisenach, A.W. Valle, D. Hardee, R.G. Gordon, M.J. Aziz, Science 349 (2015) 1529–1532.
[3] J.W. Choi, D. Aurbach, Nat. Rev. Mater. 1 (2016) 16013.
[4] B. Dunn, H. Kamath, J.M. Tarascon, Science 334 (2011) 928–935.
[5] S. Chong, Y. Wu, Y. Chen, C. Shu, Y. Liu, J. Power Sources 356 (2017) 153–162.
[6] X. Xiang, K. Zhang, J. Chen, Adv. Mater. 27 (2015) 5343–5364.
[7] X. Wu, D.P. Leonard, X. Ji, Chem. Mater. 29 (2017) 5031.
[8] N. Singh, T.S. Arthur, C. Ling, M. Matsui, F. Mizuno, Chem. Commun. 49 (2013) 149–151.
[9] C. Xu, B. Li, H. Du, F. Kang, Angew. Chem. 124 (2012) 957–959.
[10] B. Wang, Y. Han, X. Wang, N. Bahlawane, H. Pan, M. Yan, Y. Jiang, iScience 3 (2018) 110–133.
[11] Y. Wu, M. Gong, M.C. Lin, C. Yuan, M. Angell, L. Huang, D.Y. Wang, X. Zhang, J. Yang, B.J. Hwang, Adv. Mater. 28 (2016) 9218–9222.
[12] M. Peng, D. Zhang, L. Zheng, X. Wang, Y. Lin, D. Xia, Y. Sun, G. Guo, Nano Energy 31 (2017) 64–73.
[13] Y. Jiang, S. Yu, B. Wang, Y. Li, W. Sun, Y. Lu, M. Yan, B. Song, S. Dou, Adv. Funct. Mater. 26 (2016) 5315–5321.
[14] D. Yuan, X. Liang, L. Wu, Y. Cao, X. Ai, J. Feng, H. Yang, Adv. Mater. 45 (2015) 6301.
[15] P.F. Wang, Y. You, Y.X. Yin, Y.S. Wang, L.J. Wan, L. Gu, Y.G. Guo, Angew. Chem. 128 (2016) 7571–7575.
[16] Z. Li, C. Bommier, Z.S. Chong, Z. Jian, T.W. Surta, X. Wang, Z. Xing, J.C. Neuefeind, W.F. Stickle, M. Dolgos, Adv. Energy Mater. 7 (2017) 1602894.
[17] Y. Zheng, T. Zhou, C. Zhang, J. Mao, H. Liu, Z. Guo, Angew. Chem. 55 (2016) 3408–3413.
[18] X. Ge, Z. Li, L. Yin, Nano Energy 32 (2017) 117–124.
[19] W. Zhang, Y. Liu, Z. Guo, Sci. Adv. 5 (2019) 7412.
[20] J. Xu, Y. Dou, Z. Wei, J. Ma, Y. Deng, Y. Li, H. Liu, S. Dou, Adv. Sci. 4 (2017) 1700146.
[21] K. Share, A.P. Cohn, R. Carter, B. Rogers, C.L. Pint, ACS Nano 10 (2016) 9738.

[22] X. Wang, K. Han, D. Qin, Q. Li, C. Wang, C. Niu, L. Mai, Nanoscale 9 (2017) 18216–18222.
[23] Z. Jian, Z. Xing, C. Bommier, Z. Li, X. Ji, Adv. Energy Mater. 6 (2016) 1501874.
[24] I. Sultana, M.M. Rahman, T. Ramireddy, Y. Chen, A.M. Glushenkov, J. Mater. Chem. A 5 (2017) 23506–23512.
[25] W. Zhang, J. Mao, S. Li, Z. Chen, Z. Guo, J. Am. Chem. Soc. 139 (2017) 3316.
[26] I. Sultana, T. Ramireddy, M.M. Rahman, Y. Chen, A.M. Glushenkov, Chem. Commun. 52 (2016) 9279.
[27] W.D. Mcculloch, X. Ren, M. Yu, Z. Huang, Y. Wu, ACS Appl. Mater. Interfaces 7 (2015) 26158.
[28] W. Zhang, W.K. Pang, V. Sencadas, Z. Guo, Joule 2 (2018) 1534–1547.
[29] W. Zhang, Z. Wu, J. Zhang, G. Liu, N.H. Yang, R.S. Liu, W.K. Pang, W. Li, Z. Guo, Nano Energy 53 (2018) 967–974.
[30] I. Sultana, M.M. Rahman, S. Mateti, V.G. Ahmadabadi, A.M. Glushenkov, Y. Chen, Nanoscale 9 (2017) 3646.
[31] H. Gao, T. Zhou, Y. Zheng, Q. Zhang, Y. Liu, J. Chen, H. Liu, Z. Guo, Adv. Funct. Mater. 27 (2017) 1702634.
[32] Q. Li, L. Li, K.A. Owusu, W. Luo, Q. An, Q. Wei, Q. Zhang, L. Mai, Nano Energy 41 (2017) 109.
[33] P. Lian, Y. Dong, Z.S. Wu, S. Zheng, X. Wang, S. Wang, C. Sun, J. Qin, X. Shi, X. Bao, Nano Energy 40 (2017) 1.
[34] W. Wang, B. Jiang, C. Qian, F. Lv, J. Feng, J. Zhou, K. Wang, C. Yang, Y. Yang, S. Guo, Adv. Mater. 30 (2018) 1801812.
[35] C. Li, Q. Deng, H. Tan, C. Wang, C. Fan, J. Pei, B. Cao, Z. Wang, J. Li, ACS Appl. Mater. Interfaces 9 (2017) 27414.
[36] Q. Deng, J. Pei, C. Fan, J. Ma, B. Cao, C. Li, Y. Jin, L. Wang, J. Li, Nano Energy 33 (2017) 350–355.
[37] L. Xue, H. Gao, W. Zhou, S. Xin, K. Park, Y. Li, J.B. Goodenough, Adv. Mater. 28 (2016) 9608.
[38] S. Chong, Y. Wu, C. Liu, Y. Chen, S. Guo, Y. Liu, G. Cao, Nano Energy 54 (2018) 106–115.
[39] S. Chong, Y. Wu, Y. Chen, S. Guo, Z. Tai, C. Shu, Q. Tan, J. Sun, Y. Liu, Electrochem. Acta 293 (2019) 299–306.
[40] X. Wang, X. Xu, C. Niu, J. Meng, M. Huang, X. Liu, Z. Liu, L. Mai, Nano Lett. 17 (2016) 544.
[41] H. Kim, J.C. Kim, S.H. Bo, T. Shi, D.H. Kwon, G. Ceder, Adv. Energy Mater. 7 (2017) 1700098.
[42] H. Kim, D.H. Seo, J.C. Kim, S.H. Bo, L. Liu, T. Shi, G. Ceder, Adv. Mater. 29 (2017) 1702480.
[43] V. Mathew, S. Kim, J. Kang, J. Gim, J. Song, J.P. Baboo, W. Park, D. Ahn, J. Han, L. Gu, NPG Asia Mater. 6 (2014) e138.
[44] W.B. Park, S.C. Han, C. Park, S.U. Hong, U. Han, S.P. Singh, Y.H. Jung, D. Ahn, K.S. Sohn, M. Pyo, Adv. Energy Mater. 8 (2018) 1703099.
[45] H. Kim, D.H. Seo, M. Bianchini, R.J. Clément, H. Kim, J.C. Kim, Y. Tian, T. Shi, W.S. Yoon, G. Ceder, Adv. Energy Mater. 8 (2018) 1801591.
[46] Y. Chen, W. Luo, M. Carter, L. Zhou, J. Dai, K. Fu, S. Lacey, T. Li, J. Wan, X. Han, Nano Energy 18 (2015) 205–211.
[47] Z. Xing, Z. Jian, W. Luo, Y. Qi, C. Bommier, E.S. Chong, Z. Li, L. Hu, X. Ji, Energy Storage Mater. 2 (2016) 63–68.
[48] D. Su, A. Mcdonagh, S.Z. Qiao, G. Wang, Adv. Mater. 29 (2016) 1604007.
[49] M. Pasta, C.D. Wessells, R.A. Huggins, Y. Cui, Nat. Commun. 3 (2012) 1149.
[50] C.D. Wessells, R.A. Huggins, Y. Cui, Nat. Commun. 2 (2011) 550.
[51] S. Chong, Y. Chen, Y. Zheng, Q. Tan, C. Shu, Y. Liu, Z. Guo, J. Mater. Chem. A 5 (2017) 22465–22471.
[52] L. Xue, Y. Li, H. Gao, W. Zhou, X. Lü, W. Kaveevivitchai, A. Manthiram, J.B. Goodenough, J. Am. Chem. Soc. 139 (2017) 2164.
[53] C. Zhang, Y. Xu, M. Zhou, L. Liang, H. Dong, M. Wu, Y. Yang, Y. Lei, Adv. Funct. Mater. 27 (2017) 1604307.
[54] X. Bie, K. Kubota, T. Hosaka, K. Chihara, S. Komaba, J. Mater. Chem. A 5 (2017) 4325.
[55] G. He, L.F. Nazar, ACS Energy Lett. 2 (2017) 1122.
[56] J. Liao, Q. Hu, Y. Yu, H. Wang, Z. Tang, Z. Wen, C. Chen, J. Mater. Chem. A 5 (2017) 19017.
[57] J. Zheng, W. Deng, Z. Hu, Z. Zhuo, F. Liu, H. Chen, Y. Lin, W. Yang, K. Amine, R. Li, J. Lu, ACS Energy Lett. 3 (2017) 65–71.
[58] X. Wu, Z. Jian, Z. Li, X. Ji, Electrochem. Commun. 77 (2017) 54–57.
[59] Y. Hironaka, K. Kubota, S. Komaba, Chem. Commun. 26 (2017) 3693–3696.
[60] C. Vaalma, G.A. Giffin, D. Buchholz, S. Passerini, J. Electrochem. Soc. 7 (2016) A1295–A1299.
[61] Z. Zhang, M. Li, Y. Gao, Z. Wei, M. Zhang, C. Wang, Y. Zeng, B. Zou, G. Chen, F. Du, Adv. Funct. Mater. 28 (2018) 1802684.
[62] Y.H. Zhu, Y.B. Yin, X. Yang, T. Sun, S. Wang, Y.S. Jiang, J.M. Yan, X.B. Zhang, Angew. Chem. 56 (2017) 7881–7885.
[63] Y.H. Zhu, X. Yang, D. Bao, X.F. Bie, T. Sun, S. Wang, Y.S. Jiang, X.B. Zhang, J.M. Yan, Q. Jiang, Joule 2 (2018) 1.
[64] K. Sada, B. Senthilkumar, P. Barpanda, Chem. Commun. 53 (2017) 8588–8591.
[65] C. Liu, S. Luo, H. Huang, Z. Wang, A. Hao, Y. Zhai, Z. Wang, Electrochem. Commun. 82 (2017) 150–154.
[66] M. Clites, J.L. Hart, M.L. Taheri, E. Pomerantseva, ACS Energy Lett. 3 (2018) 562–567.
[67] L. Deng, X. Niu, G. Ma, Z. Yang, L. Zeng, Y. Zhu, L. Guo, Adv. Funct. Mater. (2018) 1800670.
[68] T. Deng, X. Fan, J. Chen, L. Chen, C. Luo, X. Zhou, J. Yang, S. Zheng, C. Wang, Adv. Funct. Mater. 28 (2018) 1800219.
[69] Y.H. Zhu, Q. Zhang, X. Yang, E.Y. Zhao, T. Sun, X.B. Zhang, S. Wang, X.Q. Yu, J.M. Yan, Q. Jiang, Chem 5 (2019) 168–179.
[70] N. Naveen, W.B. Park, S.C. Han, S.P. Singh, Y.H. Jung, D. Ahn, K.S. Sohn, M. Pyo, Chem. Mater. 30 (2018) 2049–2057.
[71] J.Y. Hwang, J. Kim, T.Y. Yu, S.T. Myung, Y.K. Sun, Energy Environ. Sci. 11 (2018) 2821–2827.
[72] A. Gao, M. Li, N. Guo, D. Qiu, Y. Li, S. Wang, X. Lu, F. Wang, R. Yang, Adv. Energy Mater. 9 (2019) 1802739.
[73] J. Liao, Q. Hu, J. Mu, X. He, S. Wang, C. Chen, Chem. Commun. 55 (2019) 659–662.
[74] B. Li, J. Zhao, Z. Zhang, C. Zhao, P. Sun, P. Bai, J. Yang, Z. Zhou, Y. Xu, Adv. Funct. Mater. (2018) 1807137.
[75] C. Li, J. Xue, A. Huang, J. Ma, F. Qing, A. Zhou, Z. Wang, Y. Wang, J. Li, Electrochim. Acta 297 (2019) 850–855.
[76] X. Jiang, H. Liu, J. Song, C. Yin, H. Xu, J. Mater. Chem. A 4 (2016) 16205.
[77] Y. Jiang, S. Yu, B. Wang, Y. Li, W. Sun, Y. Lu, M. Yan, B. Song, S. Dou, Adv. Funct. Mater. 26 (2016) 5315.